Imaging and component analysis of pumpkin stem tissue with simultaneous SF-CARS and TPEF microscopy

GUOZHONG HOU,[1,2] **ZHIWEI DONG,**[1] **YIFAN QIN,**[3] **ZE ZHANG,**[2] **MENG LIU,**[4] **AND YUANQIN XIA**[1,2,*]

[1] *Harbin Institute of Technology, National Key Laboratory of Science and Technology on Tunable Laser, Harbin, 150080, China*
[2] *Hebei University of Technology, Center for Advanced Laser Technology, Tianjin, 300401, China*
[3] *Key Laboratory of In-Fiber Integrated Optics, Ministry of Education, Harbin Engineering University, Harbin, 150001, China*
[4] *Hebei University of Technology, School of Science, Tianjin, 300401, China*
[*]*xiayq@hebut.edu.cn*

Abstract: A multimodal nonlinear optical imaging platform based on a single femtosecond oscillator is built for simultaneous TPEF and SF-CARS imaging. TPEF microscopy and SF-CARS microscopy is utilized for mapping the distribution of the lignin component and the polysaccharide component, respectively. Visualization of vessel structure is realized. And the relative distribution of lignin and polysaccharide of vessel structure is mapped. Two pumpkin stem tissue areas with different degrees of lignification are observed with simultaneous TPEF and SF-CARS imaging, and two types of cell walls are identified. The different distribution patterns of lignin and polysaccharide in these two types of cell walls, induced by different degrees of lignification, are analyzed in detail.

1. Introduction

Coherent anti-Stokes Raman scattering (CARS) microscopy is a significant non-labelling nonlinear optical microscopy [1–3] and has been widely used as a non-invasive microscopic technique in biological imaging, medical diagnosis, and material sciences [4–8]. Broadband CARS microscopy offers feasible solution for distinguishing different chemical components, especially the species with overlapped Raman spectra. Hence, broadband CARS microscopy is suitable for studying heterogeneous systems, such as complex cells or tissues [9]. Broadband CARS techniques can be realized with several methods, such as spectral focusing [10], multiplex excitation [11–13], and Fourier-transform [14–16]. In recent years, method of spectral focusing has attracted plenty of attention due to its prominent ability in improving spectral resolution and simplifying CARS setups [17–22].

Spectral focusing CARS (SF-CARS) microscopy was pioneered by Hellerer et al. in 2004 [23]. Matched linear chirping of the pump and Stokes pulses is required for spectral focusing and has been realized with dispersive glass blocks [24], grating compressors [23], combination of glass block and acousto-optic programmable dispersive filter [25], or spatial light modulators [17,26]. Therein, realizing matched linear chirping of the pump and Stokes pulses with highly dispersive glass blocks is the simplest way for spectral focusing and is popular in SF-CARS microscopy. SF-CARS microscopy, realized with glass blocks, has been implemented with combination of femtosecond (fs) oscillator and optical parametric oscillator [24], single femtosecond oscillator [27], combination of femtosecond oscillator and photonic crystal fiber (PCF) [28,29], and the dual-comb scheme [30]. Method of spectral focusing realizes rapid spectral scanning by simply tuning the pump-Stokes time delay [23–31]. Remarkably, the introduction of spectral focusing

in CARS microscopy allows for simplified multimodal nonlinear optical microscopy [32–35], achieving simultaneously SF-CARS imaging and other attractive nonlinear optical imaging modalities like two-photon excited fluorescence (TPEF), second and third harmonic generation.
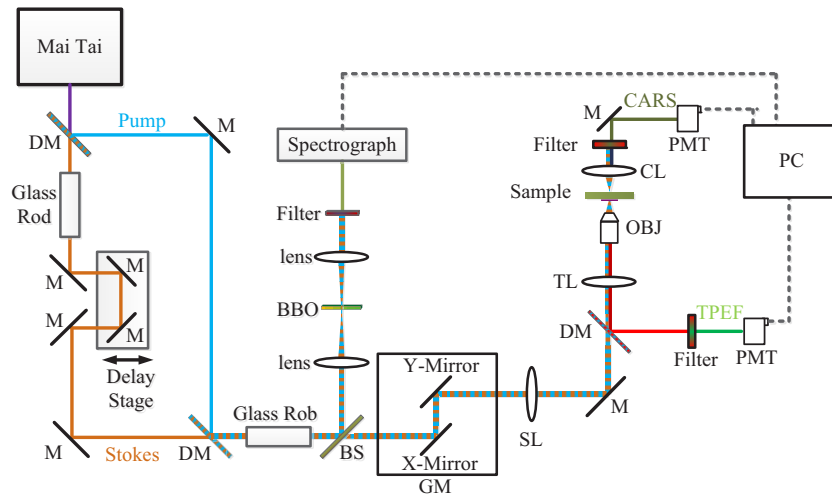
In researches of multimodal nonlinear optical microscopy, animal models or tissues from animal are widely studied [32–38]. In contrast, multimodal nonlinear optical microscopy about plants is infrequent. But research about plants is equally significant. Cell walls are the characteristic structure of the plant tissues and perform essential biological roles in process of plant growth. The functions of cell walls include regulating the shape and expansion of plant cells, controlling the tissue cohesion, exchanging ion, and defending against microbes or pathogens [39]. Cell walls are composed of organic polymers accumulated through photosynthesis. And the photosynthetically fixed carbon in cell walls makes cell walls the most abundant source of renewable energy and terrestrial biomass. Information about spatial distribution of chemical components in plant cell walls is significant for the cell wall biology and will promote the discovery of detailed mechanisms by which cell walls accomplish their particular functions and how they react in biomass conversion for producing biofuels. Given the essentiality of cell walls, various imaging techniques are explored for visualization of plant cell walls [40]. Cell walls are mainly composed of polysaccharide and lignin. Taking advantage of the Raman active vibration modes in polysaccharide and the fluorescence effect of lignin, multimodal nonlinear optical imaging of TPEF and SF-CARS is suitable for spatial distribution of chemical components in plant cell walls. In the combination of TPEF imaging and SF-CARS imaging, SF-CARS offers seletively imaging of single species at specific pump-Stokes time delay and quickly switching between species by simply tuning the pump-Stokes time delay. Therefore, the multimodal nonlinear optical imaging of TPEF and SF-CARS offers evident potential for applications in phytology.

In this research, multimodal nonlinear optical imaging of TPEF and SF-CARS is extending to application in phytology and is innovatively used to reveal the different distributions of lignin and polysaccharide, induced by different degrees of lignification, in cell walls. Multimodal nonlinear optical imaging platform based on single femtosecond oscillator is built. Simultaneous TPEF and SF-CARS imaging is demonstrated with pumpkin stem tissue. With multimodal nonlinear optical imaging of TPEF and SF-CARS, distribution of lignin and polysaccharide in the pumpkin stem tissue is mapped. Vessels are crucial structure in plant stem tissues. With simultaneous TPEF and SF-CARS imaging, vessel structure in pumpkin stem tissue is observed. Relative distribution of lignin and polysaccharide in and around the vessel structure is mapped. Two types of cell walls in pumpkin stem tissue, induced by different degrees of lignification, are distinguished through mapping the relative distribution of lignin and polysaccharide. And the distribution of lignin and polysaccharide in these two types of cell walls is analyzed in detail.

2. Experimental

The multimodal nonlinear optical imaging platform, capable of simultaneous TPEF and SF-CARS microscopy, is modified from a typical SF-CARS imaging system based on single femtosecond oscillator. Schematic diagram of the multimodal nonlinear optical imaging system is shown in Fig. 1. Single femtosecond Ti:sapphire laser oscillator (Spectra-Physics, Mai Tai, 42 MHz, 550 mW) is utilized as the excitation source of the multimodal nonlinear optical imaging system. The broadband output of the femtosecond oscillator is divided into two parts by a dichroic mirror (Semrock, FF776-Di01). The reflective part carrying short wavelength components and the transmitted part carrying long wavelength components serve as the pump pulses and the Stokes pulses in SF-CARS microscopy, respectively. The pump pulses and the Stokes pulses are spatially recombined at the second dichroic mirror of equal type. The combined beam is divided into two parts using a 2:8 beam splitter. The reflective part, with weaker power, is focused on a BBO crystal to monitor the temporal overlapping situation of the pump pulses and the Stokes

pulses. The transmitted part, with higher power, passes through the laser-scanning unit of the multimodal nonlinear optical imaging system and serves as the exciting pulses for multimodal nonlinear optical imaging. The laser-scanning unit is composed of galvo mirror (Thorlabs, GVSM002), scanning lens and tube lens. The galvo mirror consists of discrete X-axis scanning mirror and Y-axis scanning mirror, achieving laser focal spot scanning in X-axis direction and Y-axis direction. An inverted microscope (OLYMPUS IX71) equipped with a water immersion objective (Olympus, 40/0.65 160/0.17) is utilized for simultaneous TPEF and SF-CARS imaging. Distances between galvo mirror and scanning lens, scanning lens and tube lens, tube lens and objective, are set as the focus of scanning lens, the sum of focuses of scanning lens and tube lens, the sum of focuses of tube lens and objective, respectively. This optical path configuration ensures that the laser beam is limited in the aperture of the objective in the process of laser scanning. Power of the pump pulses and the Stokes pulses is set to 40 mW and 100 mW respectively at the entrance of the inverted microscope for exciting the nonlinear optical signal. TPEF signal and CARS signal, generated from the sample, are collected in the backward direction and in the forward direction, respectively. In the detection path of TPEF signal, dichroic mirror (Chroma, 680dcspxr), capable of reflecting the exciting pulses and transmitting TPEF signal, is utilized for separation of TPEF signal and the excitation background. The TPEF signal is spectrally filtered with a combination of filters (NC212066-ET670sp and BP580-70 K) and then detected by the photomultiplier tube (Hamamatsu R3896). In the detection path of SF-CARS signal, a condenser lens is utilized for collecting the forward SF-CARS signal. And the SF-CARS signal is detected by another photomultiplier tube (Hamamatsu R7422) after spectrally filtered by the two bandpass filters (FF02-675/67-25 and FF01-710/40-25). Detection windows for detecting TPEF signal and SF-CARS signal are set to 565-615 nm and 675-710 nm, respectively.

Fig. 1. Schematic diagram of the multimodal nonlinear optical imaging platform. DM: dichroic mirror, M: mirror, BS: beam splitter, BBO: Barium boron oxide, GM: galvo mirror, X-/Y-Mirror: X/Y axis scanning mirror, SL: scanning lens, TL: tube lens, OBJ: objective lens, CL: condensing lens, PMT: photomultiplier tube, PC: programmed computer.

The spectra of total output of the femtosecond oscillator, pump pulses and Stokes pulses are shown in Fig. 2(a). Peak wavelengths of the pump pulses and the Stokes pulses are 775 nm and 800 nm, respectively. The Raman region, available in the SF-CARS microscopy, is mainly determined by the full width at half maximum (FWHM) of Stokes pulses. The FWHM of Stokes pulses turns out to be about 70 nm and the corresponding wavelength components cover region of 780-850 nm. Therefore, Raman tunability of 0-1200 cm^{-1} is theoretically achievable in the

SF-CARS microscopy. To realize method of spectral focusing, two SF10 glass blocks with lengths of 2 cm and 3 cm are inserted in the Stokes path and the recombined path, respectively. A computer-controlled delay stage (Sigma Koki, SGSP20-85) in Stokes path is utilized for realizing temporal overlap of pump pulses and Stokes pulses. Spectrum of signal from BBO crystal is utilized for monitoring the temporal overlapping situation of the pump pulses and the Stokes pulses. Spectra of signal from BBO crystal under conditions of non-overlap and overlap of pump pulses and Stokes pulses are shown in Fig. 2(b). While temporal overlap of pump pulses and Stokes pulses is realized, obvious sum-frequency signal is generated from the BBO crystal.
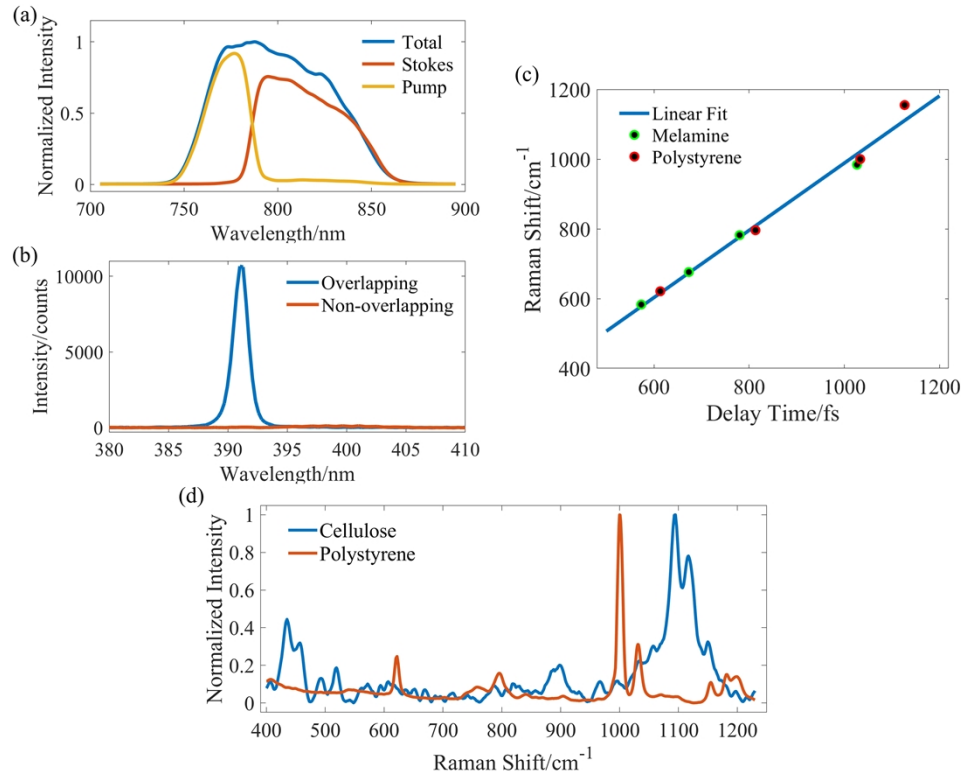
Fig. 2. (a) Spectrum of total output of the femtosecond oscillator, pump pulses and Stokes pulses. (b) Spectra of signal from BBO crystal under conditions of non-overlap and overlap of pump pulses and Stokes pulses. (c) The measured data points from melamine and PS, and the linear fitting model ($R^2 = 0.9877$). (d) Raman spectra of cellulose microcrystal and polystyrene.

In the SF-CARS microscopy, calibration of spectral scans is accomplished by comparison of the acquired SF-CARS spectra and the Raman spectra of pure melamine microcrystal and pure polystyrene (PS) beads (detailed in Supplement 1). The calibration of spectral scans is shown in Fig. 2(c). A linear fitting model is applied to the measured data points from melamine and PS for realization of CARS frequency calibration.

The mixture of pure PS beads and PS beads doped with orange fluorescent powder, and pumpkin stem tissue are prepared for multimodal nonlinear optical imaging. For multimodal imaging of the hybrid polystyrene beads and the pumpkin stem tissue, SF-CARS imaging was utilizing for imaging the PS component and the polysaccharide component, respectively. Cellulose is the dominate polysaccharide in cell walls. Raman spectra of pure PS beads and pure cellulose microcrystal in region of 0-2000 cm^{-1} are measured utilizing a portable Raman

spectrometer (BWS415-785 H, B&W Tek) to provide reference for the SF-CARS microscopy. Raman spectra of pure PS beads and pure cellulose microcrystal in region of 400-1230 cm^{-1} are shown in Fig. 2(d). The most obvious peaks in Raman spectra of pure PS beads and pure cellulose microcrystal appear at 1000 cm^{-1} and 1095 cm^{-1}, respectively.

With the multimodal nonlinear optical imaging platform, single SF-CARS or TPEF frame contains 900×900 pixels and represents a region of 135 µm × 135 µm. Single imaging frame is acquired in about 6 s with a pixel residence time of ~7 µs.

3. Results and discussion

To test the capability of the imaging platform for simultaneous TPEF and SF-CARS imaging, mixture of pure PS beads and PS beads doped with orange fluorescent powder is observed with the multimodal nonlinear optical imaging platform.

All PS beads in the mixture are transparent and monodispersed with 10 µm diameters. Due to the highly similar appearance, it's difficult to distinguish the pure PS beads and the PS beads doped with fluorescent powder by bright field microscope. The orange fluorescent powder, doped in the PS beads, can generate obvious TPEF signal in range of 550-620 nm at excitation of broadband pulses centered at 800 nm.

According to the CARS frequency calibration of SF-CARS microscopy, the pump-Stokes delay is tuned to 1020 fs to probing Raman resonance at 1000 cm^{-1} of PS molecule. For the hybrid PS beads (Supplement 1), the corresponding SF-CARS imaging is shown in Fig. 3(a). In this SF-CARS frame, six PS beads are obviously visible. The simultaneously acquired TPEF imaging is shown in Fig. 3(b). Different from the CARS frame, only two PS beads are observed in the TPEF frame. A multimodal nonlinear optical imaging, as shown in Fig. 3(c), is realized through overlapping the CARS frame and the TPEF frame. In the multimodal nonlinear optical imaging, six PS beads exist in the imaging region of 135 µm × 135 µm and two PS beads are doped with orange fluorescent powder among these six PS beads. By means of multimodal nonlinear optical imaging, two PS beads doped with orange fluorescent powder and the other four pure PS beads are distinguished successfully. The imaging results of hybrid PS beads verify that the multimodal nonlinear optical imaging platform is effective in acquiring reliable simultaneous TPEF and SF-CARS imaging.

Multimodal nonlinear optical microscopy has gotten valuable and abundant achievements with animal models or tissues. Until nowadays, studying plants with multimodal nonlinear optical microscopy is still seldom, though multimodal nonlinear optical microscopy becomes popular gradually in recent years.

Therefore, research in this letter chooses pumpkin stem tissue as the plant sample for multimodal nonlinear optical imaging and component analysis. Lignin is one of the primary components of cell walls and is an important source for generating endogenous fluorescence in plant tissues. [41,42] Another primary component of cell walls is the high molecular weight polysaccharide, including cellulose, pectic polysaccharide and hemicellulose. High molecular weight polysaccharide shares similar Raman spectrum. In the Raman spectrum of pure cellulose shown in Fig. 2(d), the most obvious Raman peak appears at around 1100 cm^{-1}. For multimodal nonlinear optical imaging of pumpkin stem tissue, TPEF microscopy is utilizing for visualization of lignin in cell walls. SF-CARS microscopy is utilizing for visualization of polysaccharide, especially cellulose in cell walls, through tuning the pump-Stokes delay to 1120 fs to probing Raman resonance at 1100 cm^{-1} of polysaccharide.

The vessel structure is observed with multimodal nonlinear optical microscopy. SF-CARS imaging and TPEF imaging of the vessel structure is shown in Fig. 4(a) and Fig. 4(b), respectively. CARS signal in Fig. 4(a) reveals the distribution of polysaccharide, as shown in Fig. 4(c). TPEF signal in Fig. 4(b) reveals the distribution of lignin, as shown in Fig. 4(d). The distribution of lignin shows the cell walls around the vessel structure. The vessel structure turns out as
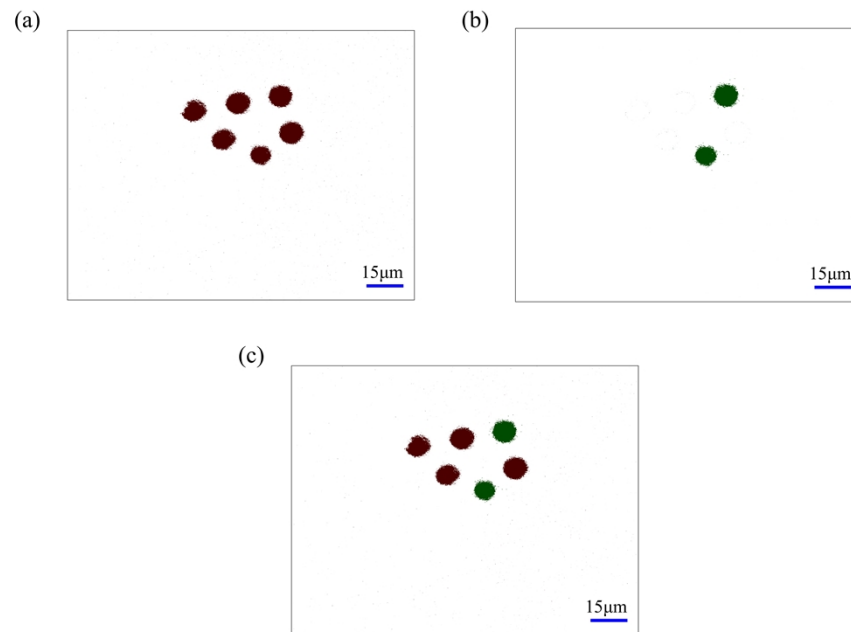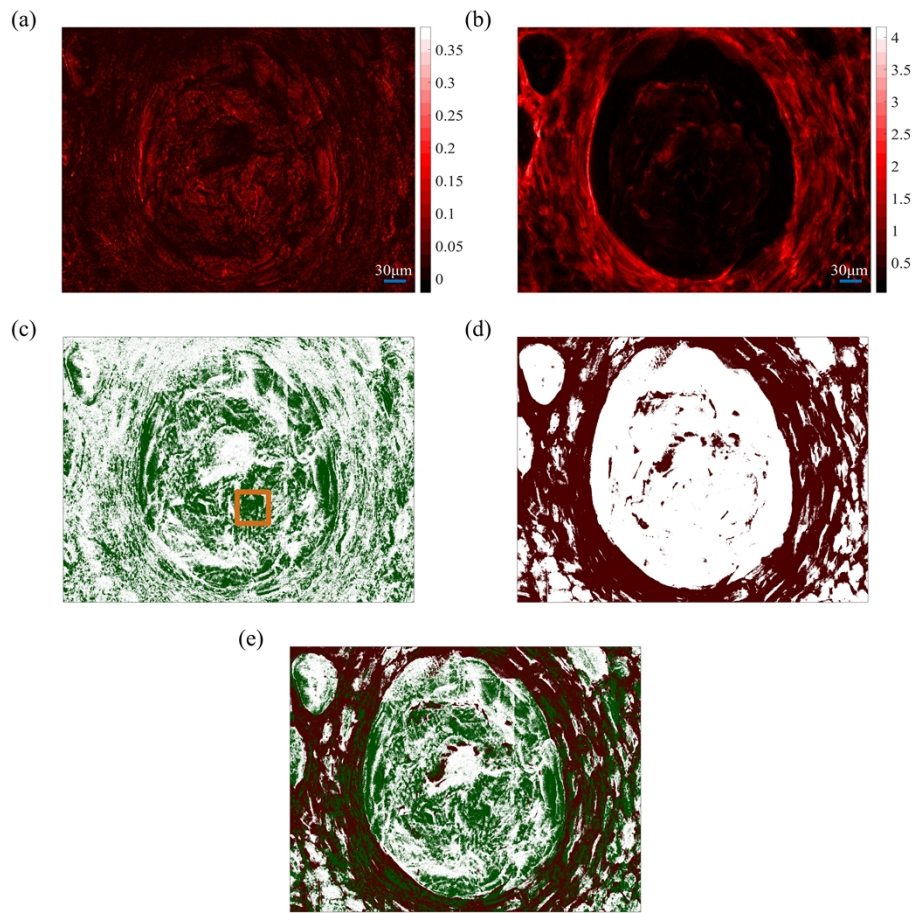
Fig. 3. Multimodal nonlinear optical imaging of mixed polystyrene beads. (a) CARS imaging. (b) TPEF imaging. (c) Multimodal nonlinear optical imaging through overlapping CARS imaging and TPEF imaging.

an obvious circle region of about 320 μm diameters in Fig. 4(c) and Fig. 4(d), formed by the distribution of polysaccharide or lignin. In the circle region of vessel structure, obvious SF-CARS signal is visible as shown in Fig. 4(c). That's to say, there is polysaccharide distributed in the vessel region of pumpkin stem tissue. Comparatively, only sporadic TPEF signal is generated from the circle region as shown in Fig. 4(d), which means nearly no lignin exists in the vessel structure. A multimodal nonlinear optical imaging, realized through overlapping the distribution of polysaccharide in Fig. 4(c) and the distribution of lignin in Fig. 4(d), is shown in Fig. 4(e), which shows the relative distribution of polysaccharide and lignin in and around the vessel structure.

With SF-CARS microscopy, the SF-CARS spectrum of polysaccharide in region labelled with orange box in Fig. 4(c) is shown in Fig. 5, acquired through tuning the pump-Stokes delay at fixed step of 6.667 fs. No lignin exists in the orange box region and therefore the SF-CARS spectrum acquired is free from interfere of lignin. Peak of the SF-CARS spectrum appears at the pump-Stokes delay of 1120 fs. According to the CARS frequency calibration, the corresponding Raman line locates at $1104 \, \text{cm}^{-1}$, consistent with the Raman peak at around $1100 \, \text{cm}^{-1}$ in the Raman spectrum of cellulose microcrystal. Overall, the SF-CARS spectrum of polysaccharide shows a high degree of consistency with the Raman spectrum of pure cellulose microcrystal shown in Fig. 2(d), which further verifies that CARS signal in Fig. 4(c) is generated from polysaccharide component.

The spatial organization of the chemical components in plant cell walls is significant for the cell wall biology and the biofuels production. Pumpkin stem tissue around vessel structures exhibits severe lignification (Supplement 1). In addition, pumpkin stem tissue near vessels exhibits high lignification degree and pumpkin stem tissue away from vessels exhibits low lignification degree, which provides natural material for studying the different distribution patterns of lignin and polysaccharide, induced by different degrees of lignification, in cell walls. Two pumpkin
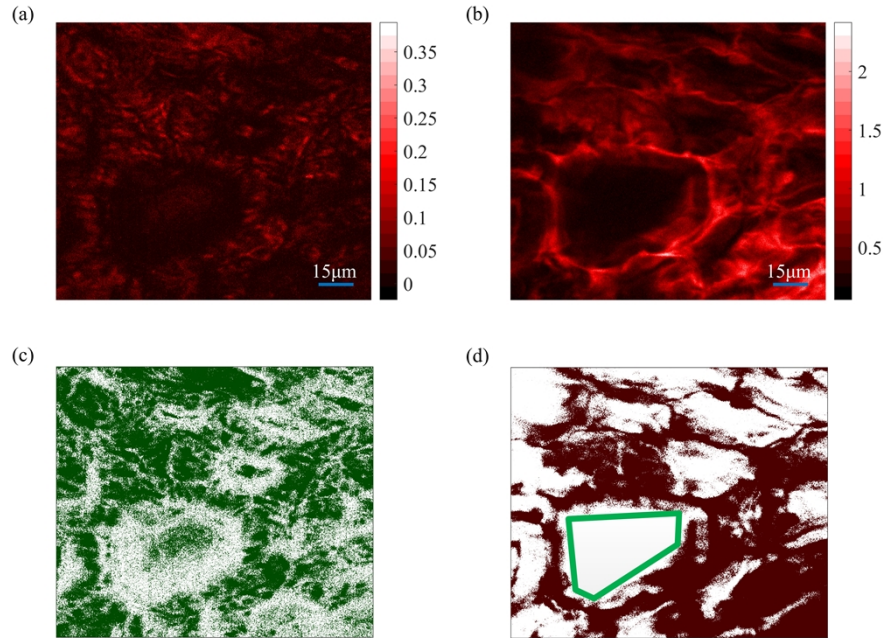
Fig. 4. Multimodal nonlinear optical imaging of vessel structure. (a) CARS imaging. (b) TPEF imaging. (c) Distribution of CARS signal in Fig. 4(a). (d) Distribution of TPEF signal in Fig. 4(b). (e) Multimodal nonlinear optical imaging through overlapping Fig. 4(c) and Fig. 4(d).
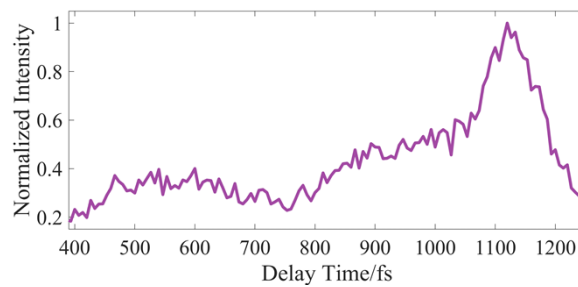
Fig. 5. Normalized SF-CARS spectrum of polysaccharide in the orange box in Fig. 4(c).

stem tissue areas, near vessel structure and away from vessel structure respectively, are chosen for simultaneous TPEF and SF-CARS imaging. For convenience of description, cell walls in pumpkin stem tissue away from vessel structure and pumpkin stem tissue near vessel structure are defined as cell wall type I and cell wall type II, respectively.

A typical CARS imaging of cell wall type I is shown in Fig. 6(a). CARS signal in Fig. 6(a) is extracted and repaint in Fig. 6(c) with green color for clearly showing the distribution of polysaccharide. TPEF imaging of cell wall type I is shown in Fig. 6(b). TPEF signal in Fig. 6(b) is extracted and repaint in 6(d) with dark red color for clearly showing the distribution of lignin. Similarly, A typical CARS imaging of cell wall type II is shown in Fig. 7(a). CARS signal in Fig. 7(a) is extracted and repaint Fig. 7(c) with green color for clearly showing the distribution of polysaccharide. TPEF imaging of cell wall type II is shown in Fig. 7(b). TPEF signal in Fig. 7(b) is extracted and repaint Fig. 7(d) with dark red color for clearly showing the distribution of lignin.
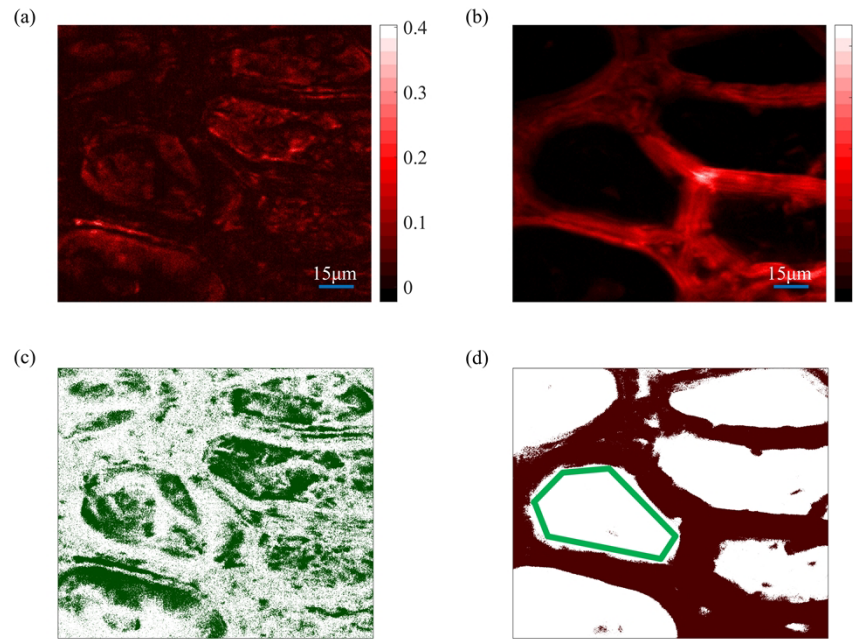

Fig. 6. TPEF and SF-CARS of pumpkin stem tissue away from vessel. (a) SF-CARS imaging. (b) TPEF imaging. (c) Distribution of CARS signal in Fig. 6(a). (d) Distribution of TPEF signal in Fig. 6(b).

In Figs. 6(a-d) and Figs. 7(a-d), the polygon shape of cells in pumpkin stem tissue is visible clearly, especially in Fig. 6(d) and Fig. 7(d). And typical polygon cells are indicated with closed green polygons as shown in Fig. 6(d) and Fig. 7(d). CARS signal in Fig. 6(c) shows that the polysaccharide in cell wall type I presents a wide ribbon distribution. TPEF signal in Fig. 6(d) shows that the lignin in cell wall type I presents a narrow strip distribution. That's to say, the distribution of polysaccharide is wider than the distribution of lignin in cell wall type I. By contrast, the distribution of lignin is wider than the distribution of polysaccharide in cell wall type II, as shown in Fig. 7(c) and Fig. 7(d). In brief, the cell wall type I is dominated by polysaccharide component and the cell wall type II is dominated by lignin component.

The multimodal nonlinear optical imaging of cell wall type I, realized by overlapping the CARS frame in Fig. 6(c) and the TPEF frame in Fig. 6(d), is shown in Fig. 8(a). In the same manner, the multimodal nonlinear optical imaging of cell wall type II is shown in Fig. 8(c). The different distribution patterns of polysaccharide and lignin in cell wall type I and in cell wall type II are more intuitive by comparison of Fig. 8(a) and Fig. 8(c). The relative distribution of polysaccharide and lignin in both cell wall type I and cell wall type II is studied through analyzing the CARS signal from polysaccharide and the TPEF signal from lignin.
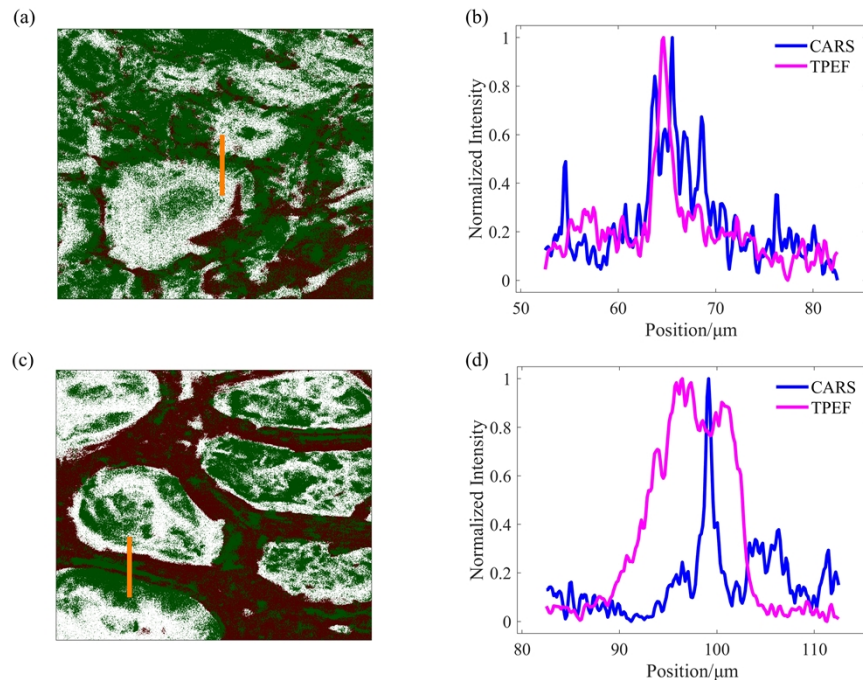
Fig. 7. TPEF and SF-CARS imaging of pumpkin stem tissue near vessel. (a) SF-CARS imaging. (b) TPEF imaging. (c) Distribution of CARS signal in Fig. 7(a). (d) Distribution of TPEF signal in Fig. 7(b).

For cell wall dominated by polysaccharide component in Fig. 8(a), the intensity curves of CARS signal and TPEF signal along the indicated orange line are shown in Fig. 8(b) with magenta and blue curves, respectively. As shown in Fig. 8(b), obvious CARS signal from polysaccharide covers range of around 63-70 µm and the TPEF signal from lignin covers range of around 63-66 µm. The single peak of TPEF signal appears amid the several peaks of CARS signal, which means that the lignin component is sandwiched by the polysaccharide component in the cell wall type I. Under this situation, the width of the cell wall is mainly determined by the width of the polysaccharide. The width of the polysaccharide component, as well as the width of the cell wall, is estimated to 7 µm and the width of lignin component in this cell wall is about 4 µm. Large area multimodal nonlinear optical imaging of pumpkin stem tissue away from vessel structure and pumpkin stem tissue near vessel structure is shown in Supplement 1.

By contrast, for cell wall dominated by lignin component in Fig. 8(c), the intensity curves of CARS signal and TPEF signal along the indicated orange line are shown in Fig. 8(d) with magenta and blue curves, respectively. The CARS signal from polysaccharide presents single peak and covers range of around 97-101 µm. And the TPEF signal from lignin covers a wider range of around 89-104 µm. It is obvious that the polysaccharide component is sandwiched by the lignin component in the cell wall type II, as indicated by CARS signal and TPEF signal in Fig. 8(d). The width of the lignin component, as well as the width of the cell wall, is estimated to 15 µm and the width of polysaccharide component in this cell wall is about 4 µm.

Cell walls in pumpkin stem tissue near vessel and pumpkin stem tissue away from vessel possess obviously different distribution patterns of lignin and polysaccharide. This difference of components in cell walls is induced by the different lignification degrees of pumpkin stem tissue near vessel and pumpkin stem tissue away from vessel. Cell walls near vessels possess a higher degree of lignification than cell walls away from vessels for the purpose of stiffening and strengthening the pumpkin stem cells and further supporting the structure of vessels. Therefore,

Fig. 8. (a) Multimodal nonlinear optical imaging of pumpkin stem tissue away from vessel realized through overlapping Fig. 6(c) and Fig. 6(d). (b) Intensity curves of CARS signal and TPEF signal along the orange line indicated in Fig. 8(a). (c) Multimodal nonlinear optical imaging of pumpkin stem tissue near vessel realized through overlapping Fig. 7(c) and Fig. 7(d). (d) Intensity curves of CARS signal and TPEF signal along the orange line indicated in Fig. 8(b).

the primary component of cell walls near vessel structure is the component of lignin, rather than the component of polysaccharide like cellulose. Briefly, the lignification increases the distribution of lignin in the pumpkin stem tissue to stiffen and strengthen the cells, as well as the vessel structures.

Although multimodal nonlinear optical imaging of TPEF and SF-CARS has acquired valuable results with animal models or human tissues [32,33], this research is the advanced attempt of multimodal nonlinear optical imaging of TPEF and SF-CARS for applications in phytology. With simultaneous TPEF imaging and SF-CARS imaging, the different distribution patterns of lignin and polysaccharide in cell walls, induced by different degrees of lignification, is revealed for the first time. Meanwhile, research in this paper needs to be further improved and deepened. In this research, the pumpkin stem tissue is observed in vitro, only TPEF imaging and SF-CARS imaging is involved in the multimodal imaging, and no method is applied to suppressing the non-resonant background in SF-CARS imaging. For the future study, live pumpkin stem tissue in vivo can be research for monitoring the dynamic distribution of polysaccharide and lignin in the lignification process or the formation process of vessel element. At the support of more PMTs, suitable filter systems, and improved control system, there is possibility for botanical research with more modalities of nonlinear optical imaging, like SHG and THG microscopy. And more components can be observed and analyzed. Besides, methods like polarization detection or frequency modulation can be utilized for non-resonant background suppression in SF-CARS imaging.

4. Conclusion

In conclusion, multimodal nonlinear optical imaging platform based on single femtosecond oscillator is built and simultaneous TPEF and SF-CARS imaging is demonstrated with pumpkin stem tissue. TPEF microscopy allows for visualization of lignin and SF-CARS microscopy realizes mapping of polysaccharide. Vessel structure of 320 μm diameters in pumpkin stem tissue is observed. Relative distribution of lignin and polysaccharide in and around the vessel structure is mapped. Two pumpkin stem tissue areas with different degrees of lignification are observed and the different distribution patterns of lignin and polysaccharide in these two types of cell walls, induced by different degrees of lignification, is revealed with simultaneous TPEF and SF-CARS imaging. Cell walls away from vessel structure, with low lignification degree, is dominated by polysaccharide. And cell walls near vessel structure, with high lignification degree, is dominated by lignin. For cell walls dominated by polysaccharide, the lignin is sandwiched by the polysaccharide. The width of the polysaccharide component, as well as the width of these cell walls, is estimated to 7 μm and the width of lignin component in these cell walls is about 4 μm. For cell walls away from vessel dominated by lignin component, the polysaccharide component is sandwiched by the lignin component. The width of the lignin component, as well as the width of these cell walls, is estimated to 15 μm and the width of polysaccharide component in these cell walls is about 4 μm. The increased distribution of lignin induced by lignification is observed in the pumpkin stem tissue.

Research in this work advances and enriches the applications of multimodal nonlinear optical imaging in phytology. The different distribution patterns of lignin and polysaccharide in cell walls, revealed with simultaneous TPEF and SF-CARS imaging, is meaningful for the cell wall biology and explaining mechanisms by which cell walls accomplish their particular functions. And this research will help promote cell walls react effectively in biomass conversion for producing biofuels.

Disclosures. The authors declare no conflicts of interest.

Data availability. Data underlying the results presented in this paper are not publicly available at this time but may be obtained from the authors upon reasonable request.

Supplemental document. See Supplement 1 for supporting content.

References

1. R. Li, X. Wang, Y. Zhou, H. Zong, M. Chen, and M. Sun, "Advances in nonlinear optical microscopy for biophotonics," J. Nanophoton. **12**(03), 1–033007 (2018).
2. V. Parodi, E. Jacchetti, R. Osellame, G. Cerullo, D. Polli, and M. T. Raimondi, "Nonlinear optical microscopy: From fundamentals to applications in live bioimaging," Front. Bioeng. Biotechnol. **8**, 585363 (2020).
3. D. Kang, R. Li, S. Cao, and M. Sun, "Nonlinear optical microscopies: Physical principle and applications," Appl. Spectrosc. Rev. **56**(1), 52–66 (2021).
4. Jr. C. H. Camp and M. T. Cicerone, "Chemically sensitive bioimaging with coherent Raman scattering," Nat. Photonics **9**(5), 295–305 (2015).
5. B. Vukosavljevic, M. Hittinger, H. Hachmeister, C. Pilger, X. Murgia, M. M. Gepp, and M. Windbergs, "Vibrational spectroscopic imaging and live cell video microscopy for studying differentiation of primary human alveolar epithelial cells," J. Biophotonics **12**(6), e201800052 (2019).
6. S. Li, Y. Li, R. Yi, L. Liu, and J. Qu, "Coherent anti-Stokes Raman scattering microscopy and its applications," Front. Phys. **8**, 598420 (2020).
7. J. Zeng, W. Zhao, and S. Yue, "Coherent Raman scattering microscopy in oncology pharmacokinetic research," Front. Pharmacol. **12**, 630167 (2021).
8. M. Rodewald, H. Bae, S. Huschke, M. T. Meyer-Zedler, A. T. Schmitt, J. Press, and Popp, "In vivo coherent anti-Stokes Raman scattering microscopy reveals vitamin A distribution in the liver," J. Biophotonics **14**(6), e202100040 (2021).
9. D. Polli, V. Kumar, C. M. Valensise, M. Marangoni, and G. Cerullo, "Broadband coherent Raman scattering microscopy," Laser Photonics Rev. **12**(9), 1800020 (2018).

10. J. G. Porquez and A. D. Slepkov, "Application of spectral-focusing-CARS microscopy to pharmaceutical sample analysis," AIP Adv. **8**(9), 095213 (2018).

11. R. A. Cole and A. D. Slepkov, "Interplay of pulse bandwidth and spectral resolution in spectral-focusing CARS microscopy," J. Opt. Soc. Am. B **35**(4), 842–850 (2018).

12. M. Nuriya, H. Yoneyama, K. Takahashi, P. Leproux, V. Couderc, M. Yasui, and H. Kano, "Characterization of intra/extracellular water states probed by ultrabroadband multiplex coherent anti-stokes Raman scattering (CARS) spectroscopic imaging," J. Phys. Chem. A **123**(17), 3928–3934 (2019).

13. Y. Arashida, A. Taninaka, T. Ochiai, H. Mogi, S. Yoshida, M. Yoshimura, and H. Shigekawa, "Low-frequency multiplex CARS microscopy with a high-repetition near-infrared supercontinuum laser," Appl. Phys. Express **14**(12), 122006 (2021).

14. K. Hashimoto, J. Omachi, and T. Ideguchi, "Ultra-broadband rapid-scan Fourier-transform CARS spectroscopy with sub-10-fs optical pulses," Opt. Express **26**(11), 14307–14314 (2018).

15. R. Kinegawa, K. Hiramatsu, K. Hashimoto, V. R. Badarla, T. Ideguchi, and K. Goda, "High-speed broadband Fourier-transform coherent anti-stokes Raman scattering spectral microscopy," J. Raman Spectrosc. **50**(8), 1141–1146 (2019).

16. F. Sinjab, K. Hashimoto, V. R. Badarla, J. Omachi, and T. Ideguchi, "Multimodal laser-scanning nonlinear optical microscope with a rapid broadband Fourier-transform coherent Raman modality," Opt. Express **28**(14), 20794–20807 (2020).

17. L. Brückner, T. Buckup, and M. Motzkus, "Enhancement of coherent anti-Stokes Raman signal via tailored probing in spectral focusing," Opt. Lett. **40**(22), 5204–5207 (2015).

18. K. Chen, T. Wu, H. Wei, and Y. Li, "Dual-soliton Stokes-based background-free coherent anti-Stokes Raman scattering spectroscopy and microscopy," Opt. Lett. **41**(11), 2628–2631 (2016).

19. M. Mohseni, C. Polzer, and T. Hellerer, "Resolution of spectral focusing in coherent Raman imaging," Opt. Express **26**(8), 10230–10241 (2018).

20. K. Tomita, Y. Kojima, and F. Kannari, "Selective coherent anti-Stokes Raman scattering microscopy employing dual-wavelength nanofocused ultrafast plasmon pulses," Nano Lett. **18**(2), 1366–1372 (2018).

21. R. A. Cole and A. D. Slepkov, "Polarization-enabled spectral-focusing CARS microscopy," OSA Continuum **3**(10), 2766–2781 (2020).

22. I. Pope, F. Masia, K. Ewan, A. Jimenez-Pascual, T. C. Dale, F. A. Siebzehnrubl, and W. Langbein, "Identifying subpopulations in multicellular systems by quantitative chemical imaging using label-free hyperspectral CARS microscopy," Analyst **146**(7), 2277–2291 (2021).

23. T. Hellerer, A. M. K. Enejder, and A. Zumbusch, "Spectral focusing: High spectral resolution spectroscopy with broad-bandwidth laser pulses," Appl. Phys. Lett. **85**(1), 25–27 (2004).

24. I. Rocha-Mendoza, W. Langbein, and P. Borri, "Coherent anti-Stokes Raman microspectroscopy using spectral focusing with glass dispersion," Appl. Phys. Lett. **93**(20), 201103 (2008).

25. M. S. Alshaykh, C. S. Liao, O. E. Sandoval, G. Gitzinger, N. Forget, D. E. Leaird, and A. M. Weiner, "High-speed stimulated hyperspectral Raman imaging using rapid acousto-optic delay lines," Opt. Lett. **42**(8), 1548–1551 (2017).

26. L. Brückner, T. Buckup, and M. Motzkus, "Exploring the potential of tailored spectral focusing," J. Opt. Soc. Am. B **33**(7), 1482–1491 (2016).

27. W. Langbein, I. Rocha-Mendoza, and P. Borri, "Single source coherent anti-Stokes Raman microspectroscopy using spectral focusing," Appl. Phys. Lett. **95**(8), 081109 (2009).

28. A. F. Pegoraro, A. Ridsdale, D. J. Moffatt, J. P. Pezacki, B. K. Thomas, L. Fu, and A. Stolow, "All-fiber CARS microscopy of live cells," Opt. Express **17**(23), 20700–20706 (2009).

29. J. G. Porquez, R. A. Cole, J. T. Tabarangao, and A. D. Slepkov, "Spectrally-broad coherent anti-Stokes Raman scattering hyper-microscopy utilizing a Stokes supercontinuum pumped at 800 nm," Biomed. Opt. Express **7**(10), 4335–4345 (2016).

30. K. Chen, T. Wu, T. Chen, H. Wei, H. Yang, T. Zhou, and Y. Li, "Spectral focusing dual-comb coherent anti-Stokes Raman spectroscopic imaging," Opt. Lett. **42**(18), 3634–3637 (2017).

31. B. C. Chen, J. Sung, X. Wu, and S. H. Lim, "Chemical imaging and microspectroscopy with spectral focusing coherent anti-Stokes Raman scattering," J. Biomed. Opt. **16**(2), 021112 (2011).

32. A. F. Pegoraro, A. Ridsdale, D. J. Moffatt, Y. Jia, J. P. Pezacki, and A. Stolow, "Optimally chirped multimodal CARS microscopy based on a single Ti: sapphire oscillator," Opt. Express **17**(4), 2984–2996 (2009).

33. A. F. Pegoraro, A. D. Slepkov, A. Ridsdale, D. J. Moffatt, and A. Stolow, "Hyperspectral multimodal CARS microscopy in the fingerprint region," J. Biophoton. **7**(1-2), 49–58 (2014).

34. Y. Li, X. Xiao, J. Guo, K. Zhao, S. Yao, L. Gui, and C. Yang, "Multimodal coherent anti-stokes Raman scattering microscopy with a supercontinuum all-fiber laser," IEEE Photonics J. **11**(2), 1–8 (2019).

35. K. P. Herdzik, K. N. Bourdakos, P. B. Johnson, A. P. Lister, A. P. Pitera, C. Y. Guo, and S. Mahajan, "Multimodal spectral focusing CARS and SFG microscopy with a tailored coherent continuum from a microstructured fiber," Appl. Phys. B **126**(5), 84 (2020).

36. R. Cicchi and F. S. Pavone, "Multimodal nonlinear microscopy: A powerful label-free method for supporting standard diagnostics on biological tissues," J. Innov. Opt. Health Sci. **07**(05), 1330008 (2014).

37. N. Mazumder, N. K. Balla, G. Y. Zhuo, Y. V. Kistenev, R. Kumar, F. J. Kao, and N. A. Krivova, "Label-free non-linear multimodal optical microscopy—basics, development, and applications," Front. Phys. **7**, 170 (2019).

38. K. König, H. G. Breunig, A. Batista, A. Schindele, M. Zieger, and M. Kaatz, "Translation of two-photon microscopy to the clinic: multimodal multiphoton CARS tomography of in vivo human skin," J. Biomed. Opt. **25**(01), 1–014515 (2020).

39. C. Somerville, S. Bauer, G. Brininstool, M. Facette, T. Hamann, J. Milne, and H. Youngs, "Toward a systems approach to understanding plant cell walls," Science **306**(5705), 2206–2211 (2004).

40. Y. Zhao, Y. Man, J. Wen, Y. Guo, and J. Lin, "Advances in imaging plant cell walls," Trends Plant Sci. **24**(9), 867–878 (2019).

41. Z. Ji, J. F. Ma, Z. H. Zhang, F. Xu, and R. C. Sun, "Distribution of lignin and cellulose in compression wood tracheids of Pinus yunnanensis determined by fluorescence microscopy and confocal Raman microscopy," Ind. Crops Prod. **47**, 212–217 (2013).

42. A. Maceda and T. Terrazas, "Fluorescence microscopy methods for the analysis and characterization of lignin," Polymers **14**(5), 961 (2022).